First results from simulations of rapid shutdown with neon deposition in J-TEXT rotating plasmas

Xin YE[1], Zhonghe JANG [1], Wei YAN [1], Yunfeng LIANG [1,2,4], Yonghua DING [1], Zhongyong CHEN [1]

[1] International Joint Research Laboratory of Magnetic Confinement Fusion and Plasma Physics, State Key Laboratory of Advanced Electromagnetic Engineering and Technology, School of Electrical and Electronic Engineering, Huazhong University of Science and Technology, Wuhan, 430074, China

[2] Southwestern Institute of Physics, Chengdu 610041, Sichuan, People's Republic of China

[3] Institute of Plasma Physics, Chinese Academy of Sciences, Hefei 230031, China

[4] Forschungszentrum Jülich GmbH, Institut für Energie- und Klimaforschung-Plasmaphysik, 52425 Jülich, Germany

E-mail: zhhjiang@hust.edu.cn

Abstract

Encapsulated Payload Pellet Injection (EPPI) has been demonstrated to be an effective method of Disruption Mitigation System (DMS) through a number of experiments and simulations in DIII-D and JET. This paper investigates the effects of plasma rotation on impurity spreading under neon EPPI. Our analysis of simulations shows that the magnetic surface stochastization has a decisive influence on the core-oriented spread of impurity. The MHD instabilities increase with impurity ionization, especially of the n = 1 component, leading to the enhancement of the local transport of impurities along the stochastic field lines. In the rotating plasma, the toroidal rotation can suppress the magnetic perturbation, and then the boundary-oriented spreading of impurities is reduced. When the pellet source is toroidally localized at the magnetic axis, the rotation can quickly flatten the toroidal distribution of impurities, resulting in a smaller maximum radiated power and a lower toroidal peek factor (TPF).

Keywords: disruption mitigation, impurity deposition, plasma rotation, toroidal peek factor

1. Introduction

Disruption mitigation system (DMS) has been studied in many tokamak devices, such as J-TEXT [1–7], ITER [8–11], DIII-D [11–18], ASDEX [19] and JET [20, 21] for locating a reliable method to mitigate the damages from major disruption. In a very short time, a huge energy release can damage the burning plasma devices: the localized heat loads hit to the plasma-facing components, and poloidal halo currents in the vacuum vessel can cause force induced mechanical

stress on the vacuum vessel wall. To solve these severe problems and dissipate the energy efficiently, a variety of methods have been developed currently on different tokamaks, including massive gas injection (MGI), shattered pellets injection (SPI) or encapsulated payload pellet injection (EPPI). It should be pointed out that although MGI has been studied for many years and has certain effects on energy dissipation, its mitigation ability is still restricted by its penetration depth. To overcome this shortcoming, SPI has been established and studied on many devices, including DIII-D [12–15, 22], JET [23], J-TEXT [1, 2]. The pellets, regarded as the solid impurity, are shot into the plasma with a high initial velocity. Compared with the conventional MGI, SPI or EPPI can deliver the impurity deeper into the plasma area and has higher assimilation [1,11, 24, 25].

Substantial studies have been carried out to explore the effect of injected pellet characteristics on disruption mitigation. The simulation results of neon core deposition have indicated that the intact outer magnetic surfaces can protect the device wall from large heat loads [12]. And shattered pellet fragments can drive the strong parallel flows that transport the impurities and governs the thermal quench [22]. But the rotation is rarely studied in the previous EPPI simulations. The rotating plasmas can provide different kinds of beneficial effects, such as confinement improvement through turbulence suppression by the shear flow [25], the screening of resonant magnetic perturbations [26] and the stability of tearing [27]. Therefore, the spreading of the injected impurity must also be affected by rotation in the plasma, it is of great significance to study the effect of rotation on impurity transport. Meanwhile, the plasma rotation has been one of the topics of major interest in the field of fusion over the last few years.

The EPPI has already been modeled by V A IZZO [28] and implanted in NIMROD. The simulations are carried out under the hypothesis of idealized delivery of the impurity payload into the plasma. The purpose of the model in this paper is to study the effect of rotation on the transport of impurities under EPPI, so this model is applicable. In the present work, we mainly look into the injection of pure neon to serve as a first probe into the interaction between the EPPI and the rotation. It should be helpful to understand the physical process of impurity spreading in the rotating plasma. The previous symmetric Ne injection simulation without rotation shows the radiated power is not distributed evenly [16], due to the asymmetric heat flux produced by the 1/1 mode. However, in the EPPI model, the payload is directly deposited more deeply in the plasma. And the rotation can significantly suppress the mode component of MHD instability[30]. Further exploration of the radiation asymmetry might reveal a better disruption mitigation.

Apart from Section 1, the paper takes the form as follows. Details of the Simulation Model will be introduced in Section 2, including the computational model, the distribution diagram of the impurity and the equilibrium parameters. In section 3, three plasma rotations are presented to investigate the entire physical process of the radial neon impurity transport. Section 4 analyzes the effect of rotation on toroidal impurity spreading and the toroidal radiation asymmetry. The discussion and summary of the paper are presented in Section 5.

2. Details of the Simulation Model

In this section, we introduce the computational model and impurity deposition distribution as well as the target equilibrium and the initial configurations setting.

2.1. Computational model

The impurity ionization, radiation and atomic physics models in the KPRAD subroutine [31] have been embedded in the main program framework of NIMROD. The combined code has been used extensively to study disruption in DIII-D [16,18,32] and J-TEXT [33]. The impurity model, all impurity species are advected by a single fluid velocity and share a single temperature. Each individual charge state of impurity is tracked and is updated at every grid point and at each time step. In the simulations, the single fluid resistive-MHD equations are presented as follows:

$$\rho \frac{\mathrm{d}\boldsymbol{V}}{\mathrm{d}t} = -\nabla p + \boldsymbol{J} \times \boldsymbol{B} + \nabla \cdot \mu\rho\nabla \boldsymbol{V}, \quad (1)$$

$$\frac{\partial \boldsymbol{B}}{\partial t} = -\nabla \times \boldsymbol{E} \quad \boldsymbol{E} + \boldsymbol{V} \times \boldsymbol{B} = \eta \boldsymbol{J}, \quad (2)$$

$$\frac{\partial n_\delta}{\partial t} + \nabla \cdot (n_\delta \boldsymbol{V}) = \nabla \cdot D_\delta \nabla n_\delta + S_\delta, \quad (3)$$

$$\frac{n_e}{\lambda - 1}\left(\frac{\partial T_e}{\partial t} + \boldsymbol{V} \cdot \nabla T_e\right) = -\nabla \cdot \boldsymbol{q} - p\nabla \cdot \boldsymbol{V} + \mathrm{Q}, \quad (4)$$

$$\boldsymbol{q} = -n\left[\chi_{\parallel} \boldsymbol{bb} + \chi_{\perp}\left(1 - \boldsymbol{bb}\right)\right] \cdot \nabla T, \quad (5)$$

Eq. (1) is the momentum equation, and the mass density and pressure are computed from all charge states of Ne and the main ions (deuterium). The continuity equation Eq. (3) is the impurity model in NIMROD, including neutral impurities and neutral ions and three body recombination. The enforced quasi-neutrality contributes to the computation of the electron density. Both the source terms $S_{\S}$ in Eq.(3) and the last term Q in Eq.(4) involves the energy loss from the radiation, ionization and recombination. The Ohmic heating is included in the single fluid temperature equation Eq. (4). And the heat flux coefficients and Spitzer resistivity, which are closely related to temperature, play an important influence on the exact simulation of thermal quench. The conducted heat flux $\boldsymbol{q}$ parameterized by parallel and perpendicular coefficients$\chi_{\parallel}(T_e) \propto {T_e}^{5/2}$ and $\chi_{\perp}(T_e) \propto {T_e}^{-1/2}$, respectively. The ergodic magnetic fields can significantly enhance radial heat flux, and the parallel heat flux coefficient is much larger than $\chi_{\perp}$.

2.2. Impurity deposition distribution

The process of payload entering the plasma region is simplified (without speed, spallation and ablation process) in the present simulations. The impurity is assumed to be deposited on a specific location (e.g. near q = 3 surface or magnetic axis). In the EPPI model, the pellet impurity is localized in a local area as seen in figure 1(a). The poloidal neutral distributions are plotted in figure 1(b).

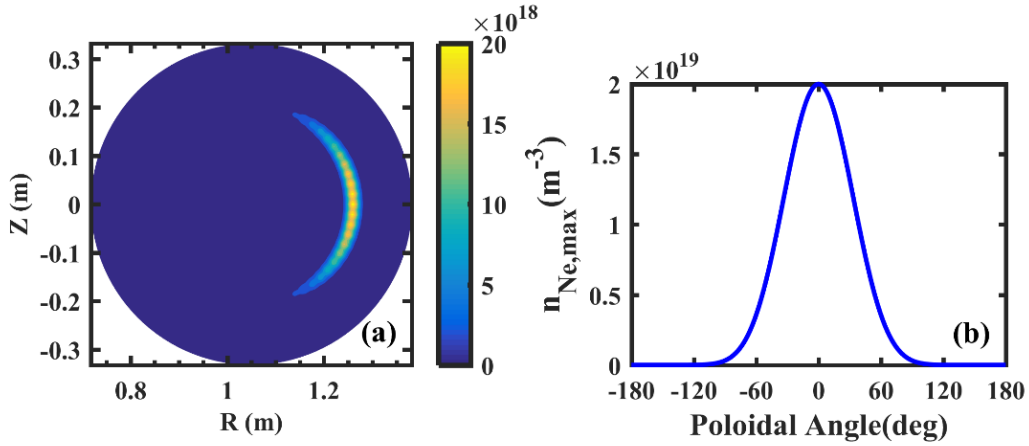

Figure 1. Impurity deposition model: (a) the impurity plume is deposited near q = 3 surface; (b) the distribution of neon impurity density in the poloidal direction.

When the payload is deposited in the core region of the plasma, the distribution of impurity in the poloidal plane is concentrated at the beginning of simulation. The model has been implemented in Ref [12]. In this case, the distribution function does not produce the above crescent shape. Figure 2 shows the 3D rendering of the shape for the deposited ionized Ne in the core area.

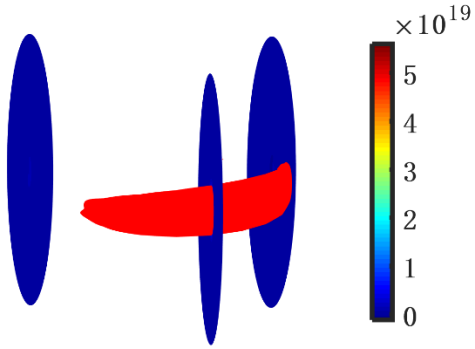

Figure 2. Color contours of ionized Ne density (plotted in three poloidal planes) shortly after the simulation is initiated, and the peak of impurity plume is deposited at 180° in toroidal angle.

Overall, there are two types of EPPI simulations in this paper: (1) the neon is deposited at the magnetic axis, as shown in figure 2; (2) the payload is placed near q = 3 surface. In both cases, the impurity not only expends in the parallel direction (driven by parallel pressure balance, as described in Refs [16, 31]), but also spreads in radial direction due to convection as the pressure and current profiles rapidly evolve. The former focuses on the influence of rotation on outward impurity mixing and toroidal radiation asymmetry.

2.3. Target equilibrium and initial configurations

The pellet impurity is deposited into a J-TEXT equilibrium based on the shot #1044192, with $q_0 = 0.97$ and $q_a = 3.59$, the toroidal magnetic field $B_t = 1.8\,\mathrm{T}$, the total plasma current $I_p = 160\,\mathrm{kA}$, central electron temperature $T_e(0) = 800\,\mathrm{eV}$, central electron density $n_e \sim 1.7\times 10^{19}\mathrm{m}^{-3}$and edge electron density $n_e \sim 1.8\times 10^{18}\ \mathrm{m}^{-3}$, The pressure at the magnetic axis is 3950 pa. To support the finite element calculation of J-TEXT poloidal cross section with NIMROD, the simulation grids are given¬121×121, and each time step is set to 2×10^{-7}s. For the two payload injection types talked above, a total of 4.7×10^{17} (at the magnetic axis, case 1) and 4.8×10^{18} (near q=3 surface, case 2) of Ne is deposited over a short time window < 0.1 ms. The mass of the background plasma is 1.25×10^{19}.

What's more, the simulations are provided with the rotation of 0 km/s, -15 km/s and -45 km/s, respectively. In NIMROD code, the plasma toroidal rotation is set by ve_0 and ve_a of the equilibrium parameters, where ve_0 represents the rotation at the plasma edge and ve_a is set at magnetic axis. The rotation appears as a gaussian distribution in the radial direction as shown in figure 3(b). The negative value of rotational velocity represents counter-current direction, and if not specifically stated, the plasma rotation refers to the toroidal rotation in this paper. Some more detailed parameters in the simulations are listed in Table 1.

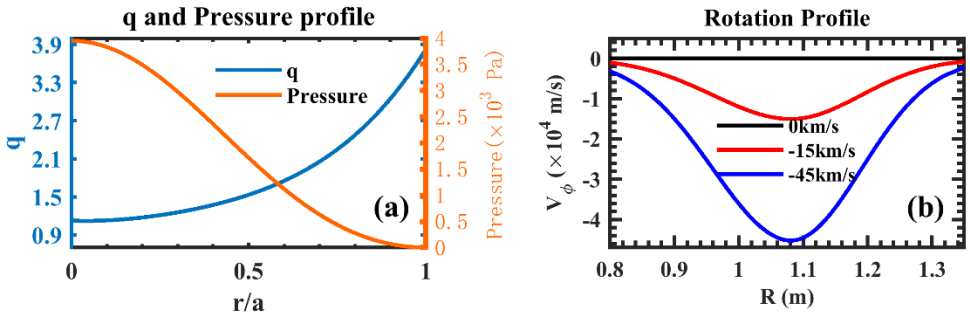

Figure 3. Initial parameter profile: (a) Initial pressure (right) and q (left) profiles, (b) Three different rotation profiles at the initial moment.

Table 1. Main input parameters in the simulations

Parameter	Position description	Value(s)	Unit
Total plasma current (I_p)	magnetic axis	160	kA
Toroidal magnetic field (B_t)	magnetic axis	1.8	T
Pressure (P)	magnetic axis	3950	pa
Safety factor(q)	plasma edge	3.49	/
	magnetic axis	0.97	
Lundquist number (S)	magnetic axis	1.019×10^7	a. u
Electron temperature (T_e)	magnetic axis	800	eV
Electron density(n_e)	plasma edge	1.8×10^{18}	m^{-3}
	magnetic axis	1.7×10^{19}	
Resistivity (η)	magnetic axis	2.45×10^{-8}	Ω·m

Perpendicular thermal diffusion ($\chi_\perp$)	plasma edge	0.1	m^2/s
	magnetic axis	1	
Parallel thermal diffusion ($\chi_\parallel$)	uniform	1×10^8	m^2/s
Kinetic viscosity (μ)	uniform	27	m^2/s
Particle diffusivity (D)	uniform	2	m^2/s
Rotation (v)	magnetic axis	0	km/s
		-15	
		-45	

3. Study of impurity radial spreading

The impurity deposition simulations on J-TEXT have been performed with NIMROD. Figure 4 displays the simulative time traces of plasma current, max temperature, internal energy and radiated power. The solid and dashed lines represent core deposition (case 1) and edge deposition (case 2), respectively. The condition of case 1 is ideal because the payload is deposited in the core at the beginning, so TQ starts at the initial moment and ends at about 1.8 ms. The plasma internal energy is lost from the beginning until the end of TQ shown in figure 4(c), and the initial 1.0 ms phase represents a rapid loss of energy by radiation as shown in figure 4(d). In case 2, the TQ is triggered at 1ms when impurity enters the core region, and the temperature begins to collapse quickly, while the duration of TQ is very short, about 0.2 ms. Most of the energy is lost rapidly around 1.0 ms. Then the resistivity increases and consequently CQ is triggered. It should be noted that this is not to compare the two deposition cases, our focus is to analyze the effect of rotation on impurity mixing and highlight key observations when the pellet impurity is deposited directly in the plasma.

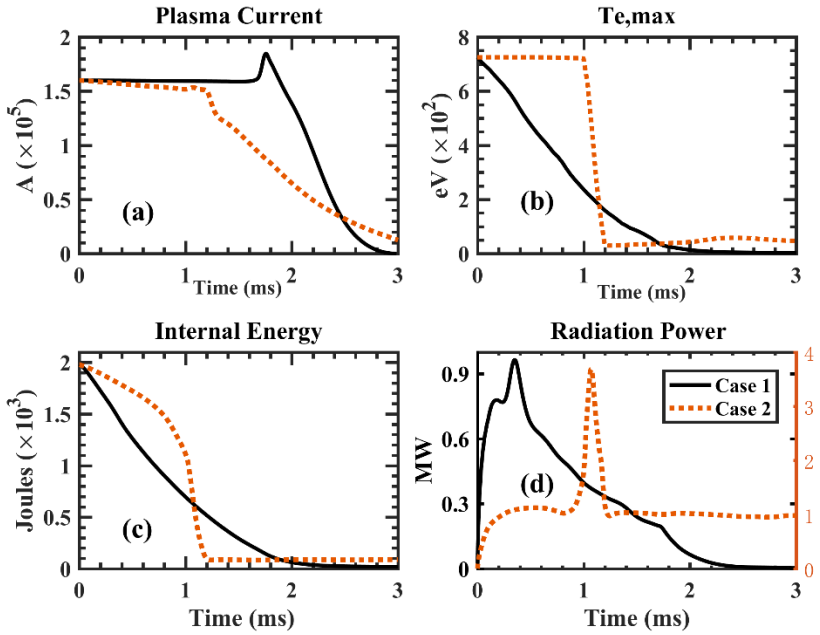

Figure 4. The time histories of the EPPI simulations without rotation: (a) plasma current; (b) T_e,max; (c) internal energy; (d) the total radiated power. Solid lines represent the core deposition

(case 1); dashed lines represent the edge deposition (case 2).

3.1. The core deposition of impurity plume

The cooling plasma and resistivity increase when the deposited neon payload spread form core to edge region of plasma, resulting in a drastic current density perturbation as shown in figure 5. The large current density profile changes can impel the magnetic perturbation of all m/n (m and n represent the poloidal and toroidal mode number, respectively) tearing modes to increase; figure 6 mainly shows the evolution of the n = 1 and n = 2 modes. As the impurity is located in the core at the initial time of simulation (t = 0), the rapid radiation cooling first flattens the central toroidal current density. With the impurity spreading from the core to the boundary in the plasma, the current density perturbation also moves outward.

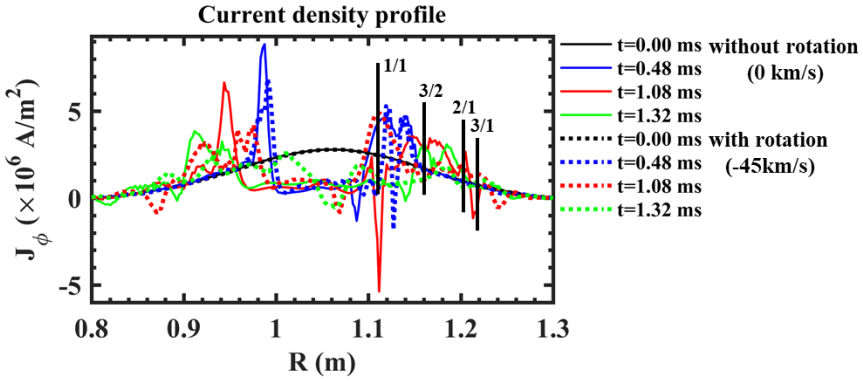

Figure 5. Toroidal current density profile in the mid-plane for the core deposition of neon impurity: the solid lines corresponding to no rotation (0 km/s); dashed lines corresponding to the rotation (-45 km/s) in the calculations. The instability increase is more evident in the case without rotation.

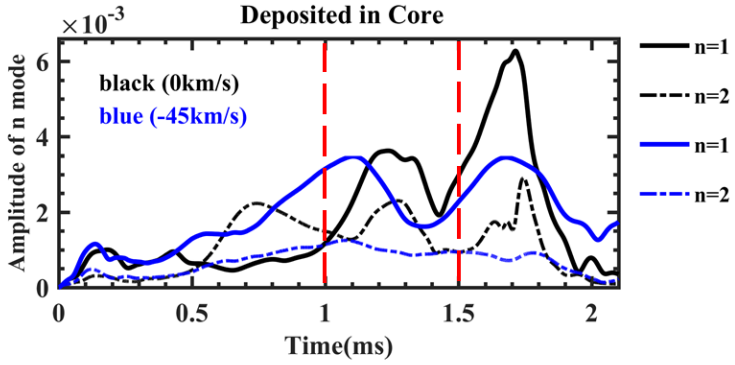

Figure 6. Amplitude of the n= 1~2 modes of $\delta B/B$ (calculated as $sqrt[W_{mag,n}/W_{mag,0}]$, where $W_{mag,n}$ is the plasma magnetic energy of the toroidal n component). The black and blue lines indicate the rotation of 0 km/s and -45 km/s, respectively, and the solid line is n = 1, the dashed line is n = 2.

As shown in figure 6, the instability modes driven by the current perturbation undergoes

multistage increase and decline. The process is similar to the previous MGI simulations with a small amount of argon impurity injection [33]. Since the rotation of -15 km/s is calculated as a transition, the simulation under 0 km/s (the black line) and -45 km/s (the blue line) is mainly analyzed here. The simulation results without considering rotation are described first. At 0.48 ms, the gradient of current density becomes very high at the q = 1 surface marked with a blue solid line in figure 5, then the outward perturbation (q = 3/2 surface) motivates the n = 2 mode to grow rapidly and reaches a local maximal perturbation amplitude at 0.75 ms. Subsequently, the current density perturbation is intensified at the q = 2 flux surface at around 1.0 ms as shown in figure 5, and the n = 1 mode starts to grow and dominate in the late period. These conditions excite the formation of 2/1 magnetic island as shown in figure 7. Simultaneously, a weak 3/2 and 5/2 tearing modes can be observed near the q = 2 surface.

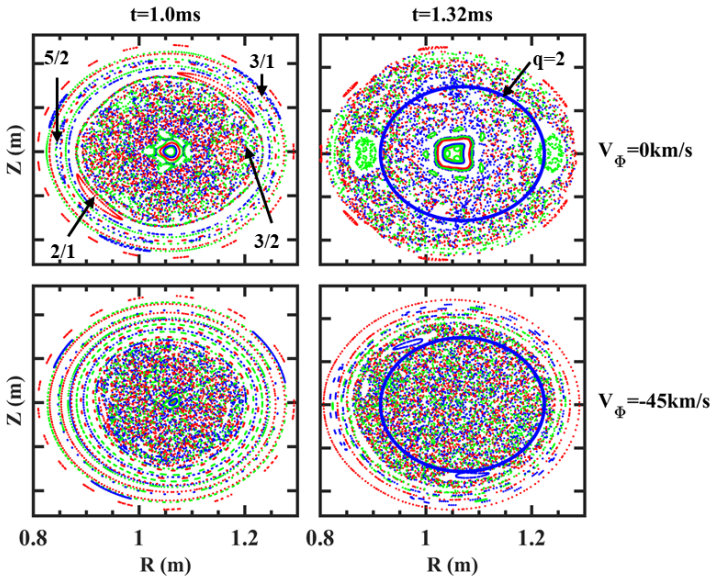

Figure 7. The magnetic topology is shown at several different moments by Poincaré plots in the cases with rotation of 0 km/s and -45 km/s. Time points 1.0 ms and 1.32 ms. The q = 2 surface is marked with the blue circle.

Both the increasing magnetic perturbation and the enlarging magnetic islands can cause the stochastic structure of the magnetic topology, and the destroyed magnetic surfaces have a great effect on the impurity spread along stochastic field lines [33]. Figure 8(a) shows the time evolution of ionized impurities and n=1 magnetic perturbation in different magnetic surfaces. The related time evolution of radial temperature distribution is displayed in figure 8(b). There are three moments marked with t_1, t_2 and t_3 corresponding to the time points in figure 8(a).

Impurity injection cooling at the initial moment of calculation can destroy the core magnetic surfaces directly, leading to a large amount of neon impurity transport out. In the figure 8(a), the

temporal correlation between the MHD growth and the impurity ionization is complicate. In the initial stage, the ionized impurities are concentrated inside q=1 magnetic surface, so the amount of ionized impurities inside of the q=1, 2 and 3 surfaces is same. However, the amount of ionized impurities inside of q=1 surface quickly reaches a peak and begins to decrease, this is from the spreading of the core ionized impurities to the boundary region through q=1 surface. Therefore, the cooling effects of ionized impurities trigger the MHD instabilities of n=1 and it is mainly related to m/n =1/1, so the magnetic perturbation is also increased accordingly at $t=t_1$, but its amplitude is limited. At the moment of $t=t_2$, the amount of ionized impurities inside of q=2 surface begin to decrease, it indicates that the ionized impurities inside of q=2 surface trigger the instability of m/n =2/1, and the magnetic perturbation begin to rise and reach another peak. In much the same way, the amount of ionized impurities inside of q=3 surface is decreased and the m/n =3/1 mode is triggered. With the development of MHD instabilities, the multimode coupling and the stochasticity of the magnetic surface are destined to happen, the impurity transport increases and the amplitude of MHD instabilities reaches the maximum at $t = t_3$.

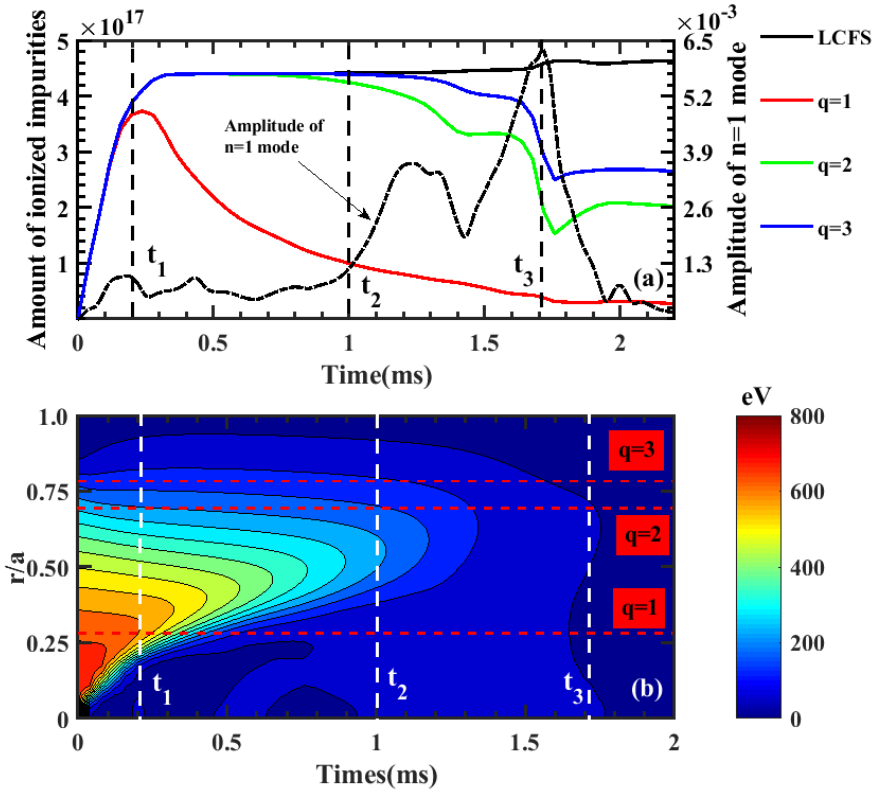

Figure 8. The process of radial impurity transport and temperature collapses in the case without rotation: (a) the time evolution of n =1 magnetic perturbation and ionized impurities number inside q = 1, q = 2 and q = 3 surface; (b) the time evolution of radial temperature distribution (corresponding surfaces are marked with red dashed lines from bottom to top). The three time points labeled by t_1, t_2 and t_3 are 0.2 ms, 1.0 ms and 1.7 ms, respectively.

For the rotating plasma, the rotation can improve the confinement performance of plasma and

suppress the non-ideal MHD instability [30]. In the case with rotation, the current density perturbation marked with dashed lines is lower at the same time as shown in figure 5. The stabilizing effect of rotation is likely to have great influence on the radial transport of impurity. As the maximal peak values of the n = 1 and 2 modes of the magnetic perturbation and its growth rate are smaller, as shown in figure 6. The magnetic surfaces are maintained more completely than the case without rotation as displayed by figure 7. Therefore, the spread of radial impurity is weaker.

The evolution comparison of impurity fraction inside q = 2 surface under different rotations is shown in figure 9(a) in which the rotation of -15km/s is regarded as a transitional analysis. At 1.0 ms, the neon impurities are transported near q = 2 surface. The amplitude of the excited magnetic perturbation reaches the peak for the first time at 1.2 ms (as shown in figure 6), which may trigger a minor disruption and destroy the nearby magnetic surface (as shown in figure 7). Later, a little impurity crosses the q = 2 surface, and the fraction begins to decline slowly. When the outermost closed magnetic surface is stochastic, the change rate of the impurity fraction reaches the peak, indicating that the radial impurity transport at this time is the strongest. Figure 9(b) is the corresponding derivative of impurity fraction. Because the rotation can improve the MHD stability as mentioned in [30], the peak values of derivative at -15 km/s and -45 km/s are postponed by about 0.3 ms and 0.6 ms, which is labeled by the second and third vertical dashed lines, respectively. The boundary temperature is maintained longer accordingly. Therefore, the stability effect of large rotation is more significant, which is not conducive to the perpendicular transport of impurities along the stochastic magnetic field lines. The growth of the magnetic perturbation caused by the impurities confined in the core starts earlier as shown in figure 6. The strong time correlation between the impurity fraction variation and the stochasization of the magnetic topology indicates that the radial impurity transport originates from the growth of MHD instabilities.

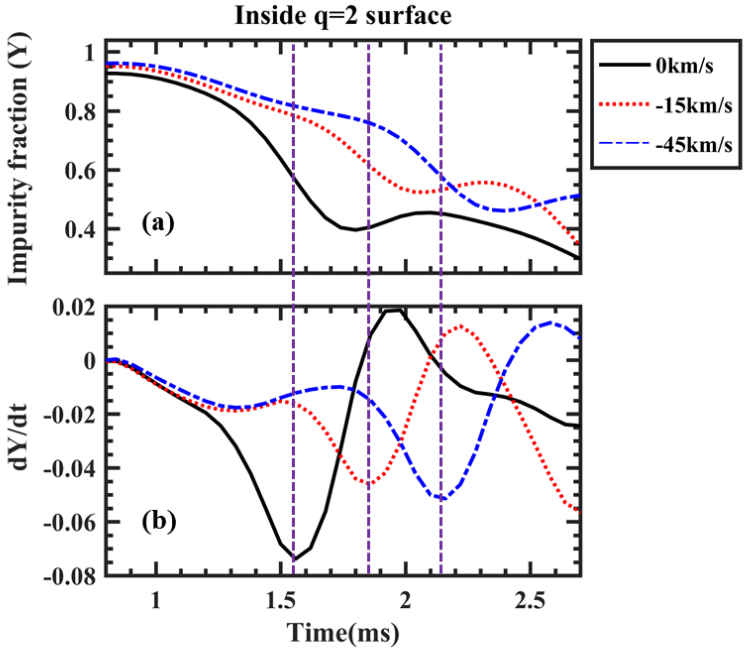

Figure 9. The neon impurity fraction (a) and its time derivative (b) inside q = 2 surface for the simulations with the rotation of 0 km/s, -15 km/s and -45 km/s. The greater the rotation, the stronger the stabilization effect, which can better maintain the integrity of the q=2 magnetic surface, the moment when the impurity quickly escapes from the q=2 surface will also be delayed. Therefore, when the rotation is large, the content of magazines confined in the q=2 surface is relatively more.

3.2. The edge deposition of impurity plume

The impurity plume is deposited directly near the boundary of the plasma, close to the q = 3 surface. Radiant cooling due to ionization of impurities will also excites the current density perturbation as shown in figure 10. First, let's discuss the calculation results without rotation. As the impurities diffuse from the boundary to the inside, a weak current density profile perturbation occurs in sequence at the q = 3 and q = 2 surfaces (as shown in figure 10(a)). Then, the n = 1 component of magnetic perturbation starts to grow rapidly at about 0.5 ms shown in figure 11, leading to the destabilization of the 2/1 and 3/1 tearing mode. When the size of the magnetic island exceeds a certain threshold, the corresponding magnetic surfaces become stochastic in figure 12(top). From figure13, the local transport of impurities is enhanced in the radial direction at this moment, and the fraction of impurity inside the q = 3 and q = 2 surface increases rapidly. Substantially, the impurities are transported further to the core region, and the current density channel shrinks severely as shown in figure 10(b). The gradient of the current density and magnetic perturbation reach the maximum and the whole magnetic surface is stochastic at 1.0 ms. Then, the impurities enter the q = 1 surface marked with the red line in figure 13. Nonetheless, there are still a few impurities diffusing into the vacuum area, resulting in a short-term decline in the fraction inside q = 2 and q = 3 surface at 1.15 ms as shown in figure 13.

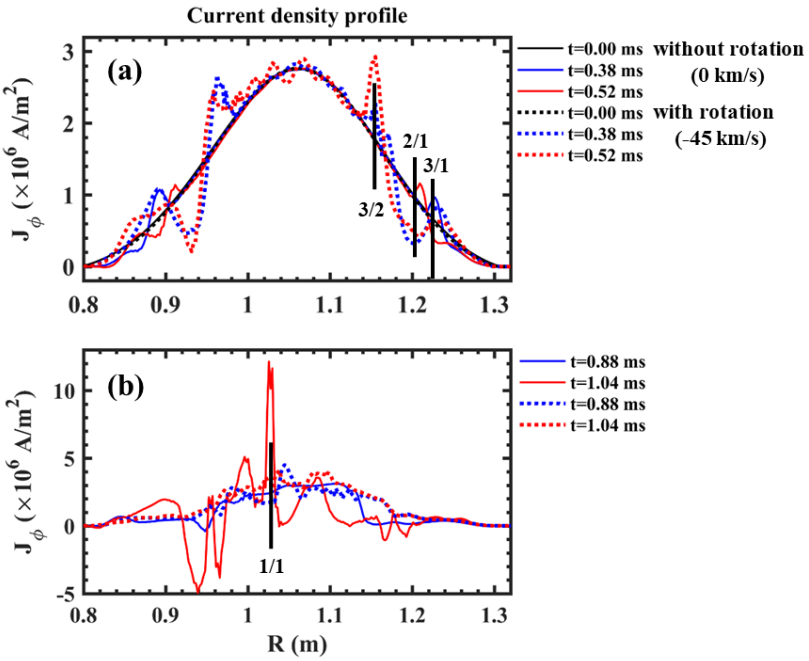

Figure 10. The mid-plane toroidal current density profile for the edge deposition of neon impurity: (a) before the thermal quench; (b) the thermal quench stage. The solid lines and dashed lines correspond to no rotation (0 km/s) and the rotation (-45 km/s) respectively.

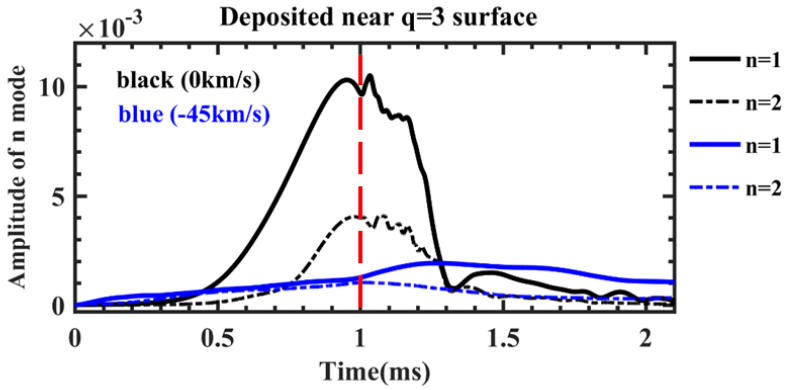

Figure 11. Amplitude of the n= 1~2 modes of $\delta B/B$. The black and blue lines indicate the rotation of 0 km/s and -45 km/s, respectively, and the solid line is n = 1, the dashed line is n = 2.

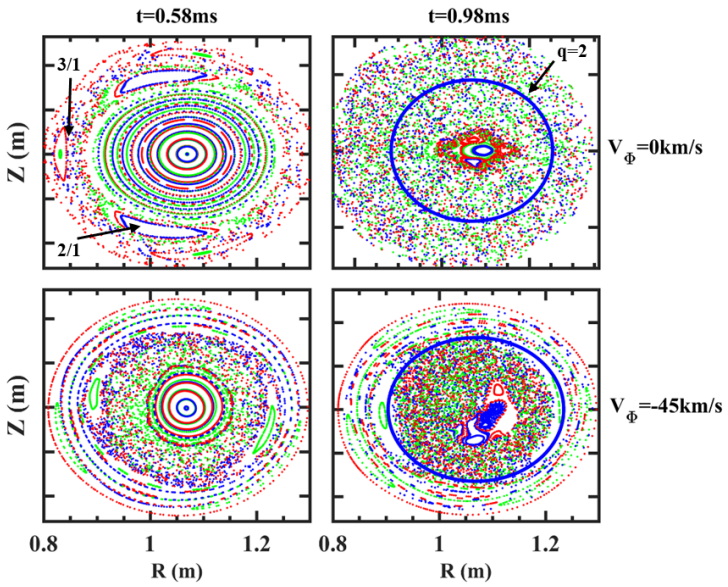

Figure 12. The magnetic topology is shown at several different moments by Poincaré plots in the cases with rotation of 0 km/s and -45 km/s. Time points 0.58 ms and 0.98 ms. The q = 2 surface is marked with the blue circle.

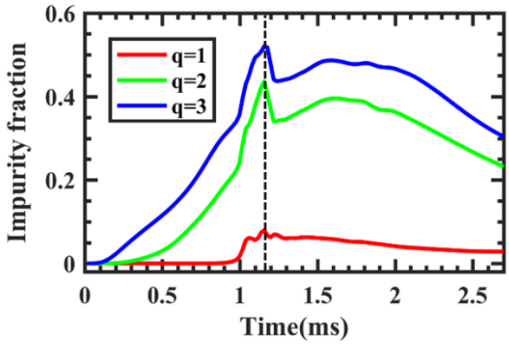

Figure 13. The time evolution of neon impurity fraction inside q = 1, q = 2 and q = 3 surface in the case without rotation.

However, when the toroidal rotation (-45 km/s) is considered, the current density gradients at q = 2 and q = 3/2 surface are greater before the thermal quench as seen in figure 10(a). The stochasization between the two magnetic surfaces is also more serious at 0.58 ms as shown in figure 12 (bottom). The reason why the core and boundary magnetic surfaces remain intact is probably the interaction between the current density perturbation and rotation stabilization; the initial impurity cooling leads to a high gradient of the current profile at the deposit site, where the magnetic surfaces are first destroyed, and due to the suppression of magnetic perturbation by rotation as shown in figure 11, other magnetic surfaces can be maintained intact. Even at 0.98 ms, the boundary magnetic surfaces are still intact (figure 12). These conditions help impurities enter the q=2 plane faster shown in figure 14. Soon, the fraction reaches saturation at about 0.5 ms.

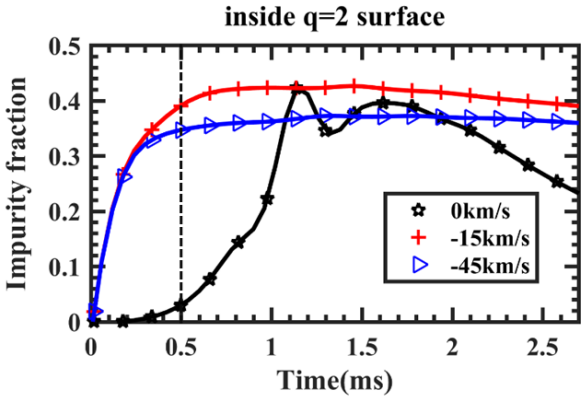

Figure 14. The neon impurity fraction inside q = 2 surface for the simulations with the rotation of 0 km/s, -15 km/s and -45 km/s.

Based on the above analysis of the two impurity deposition models. It can be concluded that the magnetic surface stochasization has a decisive influence on the enhancement of the radial transport of impurities. However, the suppression of MHD instability by rotation can maintain the magnetic surface well, which is not conducive to local impurity transport.

4. Toroidal radiation asymmetry under the core deposition of neon impurity

4.1. Toroidal spreading of impurity

Here, we pay more attention to the impurity spread when the neon impurities are deposited at the core region. At the initial time of calculation, the impurity plume is deposited on axis with a 2D Gaussian profile in the poloidal plane having a 0.6 cm half width and is elongated in the toroidal direction with a 0.6 m half as shown in figure 2. The intuitive state of the distribution of impurities by three poloidal planes of toroidal angle: 30°, 180° and 270° is shown in figure 15. In the case without equilibrium rotation, the impurity peak is consistently at a fixed toroidal position. However,

if the rotation is considered in the calculations. From the bottom of figure 15(a), the toroidal impurity distribution changes significantly in the rotating plasma with the rotation of -45 km/s, and the impurity density is almost distributed in the entire toroidal space. One possible reason is that the

$\boldsymbol{V}\nabla\cdot n_s$ from $\nabla\cdot(n_s\boldsymbol{V}) = n_s\nabla\cdot\boldsymbol{V} + \boldsymbol{V}\nabla\cdot n_s$ (as seen in the continuity equation Eq. (3)) is not equal to 0 when the impurity density is uneven in the toroidal direction; the $\boldsymbol{V}$ includes the particle flow velocity and rotational velocity[29]. And this term will gradually change the toroidal distribution of impurities.

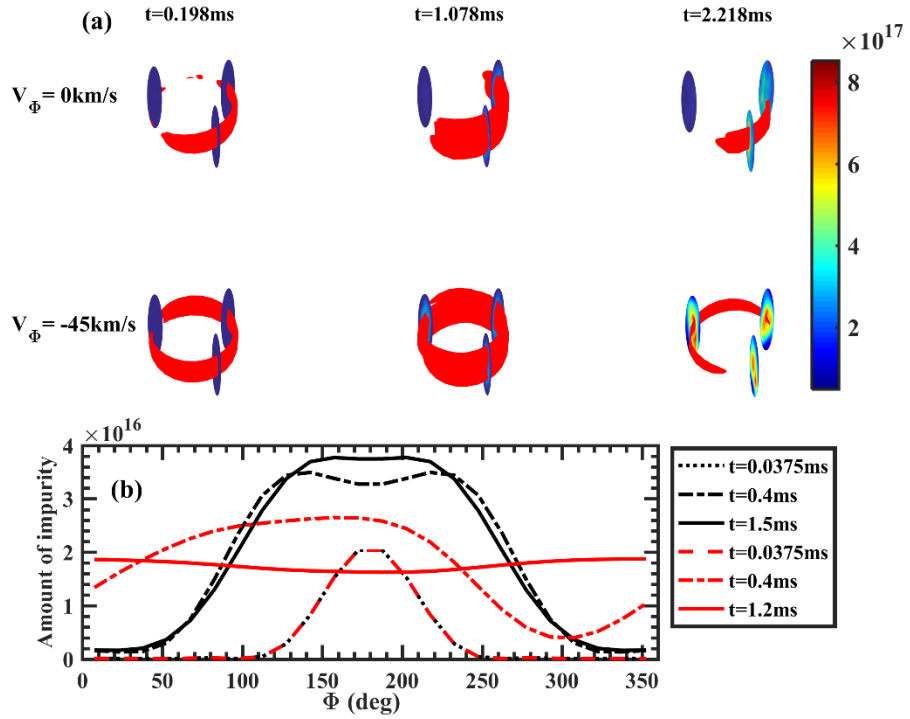

Figure 15. (a) Color contours of ionized Ne density (in units of m^{-3}) are plotted on three poloidal planes of toroidal angle: 30°, 180°, 270°. Time points 0.198, 1.078 and 2.218 are shown (all times in milliseconds). The injection location (180°) is the second plane (form left to right). The isosurface is plotted in 3D with a density of $8\times10^{17}\,m^{-3}$. (b) Evolution of toroidal distribution about ionized Ne quantity during the TQ; black and red lines represent the simulations with rotation of 0 km/s and -45 km/s respectively.

Figure 15(b) shows the corresponding evolution of the toroidal impurity quantity. At the beginning of simulations, the ionized impurity is mainly concentrated at a certain toroidal location (as plotted by solid line). Subsequently, the rotation quickly flattens the toroidal impurity distribution marked with the red lines shown in figure 15(b), maintaining about 2×10^{16}. In the calculation without rotation, the great mass of impurities is localized around 180 degrees, and the range of concentration becomes wider due to the impurity diffusion. Then the neutral Ne continues to ionized, resulting in the increase of impurity mass at the local region.

4.2. Effects of rotation on impurity radiation

The disruption mitigation system is to actively inject a large amount of impurity (such as neon, argon, deuterium, etc.) and generate enough radiated power to dissipate the energy of plasma [34]. The dissipated internal energy should be high enough at TQ ($E_{rad}/E_{th} > 90\%$, E_{rad} is the radiation energy and E_{th} is the plasma internal energy). Concurrently, to ensure the heat flux deposited on the first wall is lower than the melting limit of the material [8], the distribution of radiation should be as even as possible (both toroidal and poloidal asymmetry

factors should be less than 2).

In the first part of Section 4, we have discussed that the rotation plays an important role on the toroidal impurity spread. But the previous MGI results confirms that the more uniform impurity delivery will not always lead to more uniform radiated power [16]. In the current EPPI model, impurities are directly deposited more deeply in the plasma without diffusion through the vacuum. Meanwhile, the toroidal distribution of core impurities can be flattened by rotation shown in figure 15(b). And the rotation can significantly reduce the level of magnetic perturbation, which can affect the radiation asymmetry. The toroidal peaking factor is defined as

$$TPF(t) = \frac{\max\{P_{rad}(t,\varphi_i)\}}{\text{mean}\{P_{rad}(t,\varphi_i)\}} \qquad (i \text{ is for toroidal positions}),$$

where $P_{rad}(t,\varphi_i)$ is the total radiated power in each toroidal location by integrating over the whole poloidal cross section and assuming toroidal uniformity [35].

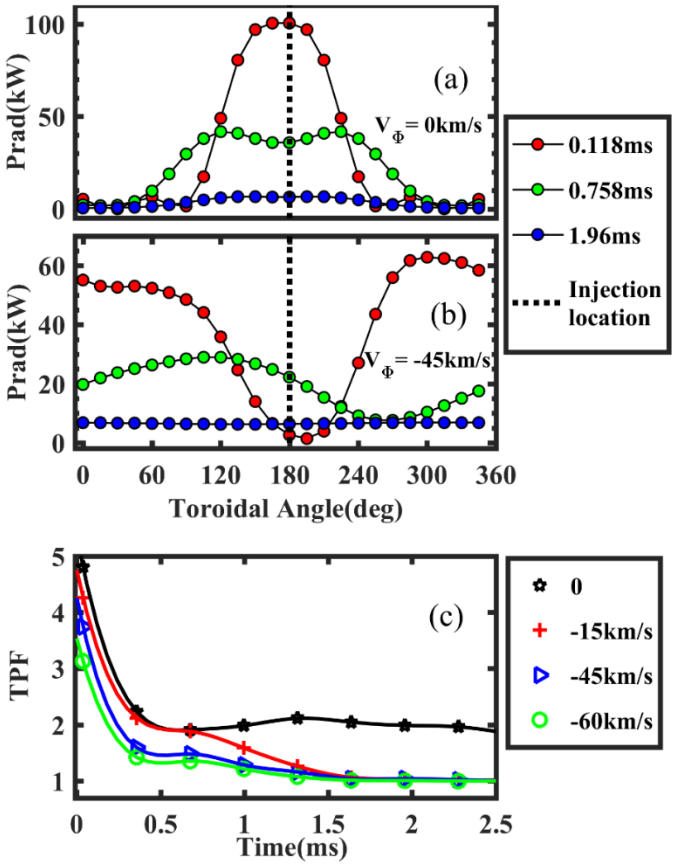

Figure 16. Distribution of toroidal radiated power during the TQ for the two simulations with rotation: (a) 0 km /s, (b) -45 km/s. The injection location is plotted by the dashed line. (c) The radiation asymmetry in the simulations with rotation of 0 km/s, -15 km/s, -45 km/s and -60 km/s.

In this study, the radiated power is obtained by calculating the volume integral of the emissivity in each 1/24 toroidal section of the plasma. From figures 16(a-b), the results show that the radiated power distribution is roughly consistent with the impurity distribution in toroidal

direction (as seen in figure15(b)), but the toroidal maximum radiated power is smaller in the rotating plasma. Figure 16(c) shows the time evolution of TPF in the simulations with different rotation. In the case with rotation of 0 km/s, the value of TPF eventually reaches to 2. However, the radiation peaking factor declines quickly and tends to be equal to 1 faster in the calculations with larger rotation.

What's more, the influence of rotation (-60 km/s) on TPF is simulated and predicted for the J-TEXT device, we find that this rotational velocity is not significantly different from -45 km/s as seen in figure 16(c). The most likely reason is that the effect of rotation on the toroidal distribution of impurities has reached saturation.

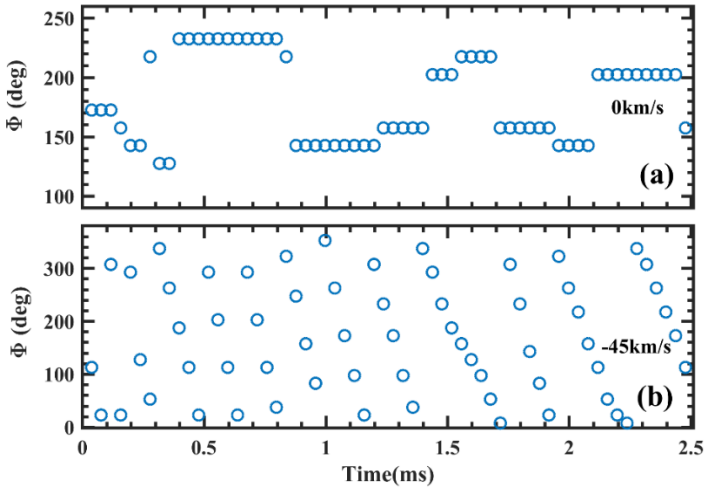

Figure 17. Toroidal position of the radiation peak: (a) without rotation; (b) with the rotation of -45 km / s.

The variation range of the toroidal radiation peak position is shown in figure 17. When the rotational velocity is 0 km/s, the position of the maximum radiated power is always around 180°, where a large amount of heat flux hits the device wall. In the case with rotation of -45 km/s, the toroidal position of radiation peak moves quickly due to the movement of the impurity peak, avoiding the local deposition of heat loads, thereby protecting the device.

5. Discussion and summary

Unlike the MGI simulations, the impurity is deposited directly in the plasma, and the assimilation of the injected material is by design 100%. We find that whether the payload is deposited in the core region or near the q = 3 surface in the plasma, the injected impurities are more easily confined inside the q = 2 magnetic surface in the simulations with rotation. The stochasization of the magnetic surface has a decisive effect on the radial spreading of impurity. The radial transport of impurities along the stochastic field lines will be enhanced in the stochastic region. However, in the rotating plasma, the toroidal rotation can suppress MHD instability[30] caused by radiative cooling. The magnetic surfaces can be protected better when the level of

magnetic perturbation is very low, and especially the n = 1 component of instability plays a greater influence. It is found that the stabilizing effect of rotation is not conducive to the radial transport of impurities, and the injected impurities can be well confined in the q = 2 surface during TQ, thereby improving the mixing efficiency of impurities in the plasma.

Furthermore, the rotation can quickly flatten the toroidal distribution of impurities, and the ionized impurities are evenly distributed in the toroidal direction. But the radiation peaking still exists as seen in figure 16(b). The previous MGI simulation of symmetric neon injection shows the same results [16]. Nevertheless, the difference of TPF remains between the preceding MGI and the current EPPI calculations. In the case of a perfectly toroidally symmetric MGI simulation [16], TPF of two is found. The uniform impurity distribution is found to produce asymmetric radiated power, due to the asymmetric heat flux produced by the 1/1 mode. However, in this study, we have considered the effect of rotation, and the injected impurities are deeper in the plasma. From the above analysis, the rotation has a significant suppression of the n = 1 mode, and the asymmetric heat flux probably does not exist in the simulations with rotation, resulting in the TPF of 1 is obtained.

Last but not least, it is believed that rotating plasma can reduce thermal deposition hazards for impurity injection. These simulation results have a certain guiding significance for the formulation of the upcoming experiment. In the future work, with the continuous improvement of the pellets injection model, the detailed study for the effect of rotation on heat flux is interesting and worth further investigation.

Xin Ye received the Master's degree from the International Joint Research Laboratory of Magnetic Confinement Fusion and Plasma Physics, State Key Laboratory of Advanced Electromagnetic Engineering and Technology, School of Electrical and Electronic Engineering, Huazhong University of Science and Technology, Wuhan, 430074, China, in 2020.
His research interests include the Encapsulated Payload Pellet Injection (EPPI) for Disruption Mitigation System (DMS) in tokamak device.

Zhonghe JANG received the Ph.D. degree from the School of Electrical and Electronic Engineering, Huazhong University of Science and Technology, Wuhan, 430074, China, in 2004. He is currently a Professor with the International Joint Research Laboratory of Magnetic Confinement Fusion and Plasma Physics Technology, Huazhong University of Science and Technology. And he is involved in MHD instability and disruption mitigation of tokamak plasma.

Acknowledgments

The authors deeply appreciate the assistance from the J-TEXT team and the NIMROD team, and the helpful advice from V.A. Izzo, Z.F. Lin, P. Shi and Y.J. Cai during the entire research period. This work was supported by the National Key R&D Program of China under Grant No. 2018YFE0309100 and by the National Natural Science Foundation of China under Grant No. 12175078.

Corresponding author is Zhonghe Jiang, He is currently a Professor with the International Joint Research Laboratory of Magnetic Confinement Fusion and Plasma Physics Technology, Huazhong University of Science and Technology. His email is zhhjiang@hust.edu.cn.

References

[1] Li Y, Chen Z Y, Wei Y N, Tong R H, Yan W, Lin Z F, Yang Z J and Jiang Z H 2018 Design of a shattered pellet injection system on J-TEXT tokamak Review of Scientific Instruments 89 10K116

[2] Luo Y H, Chen Z Y, Tang Y, Wang S Y, Ba W G, Wei Y N, Ma T K, Huang D W, Tong R H, Yan W, Geng P, Shao J and Zhuang G 2014 Designing of the massive gas injection valve for the joint Texas experimental tokamak Review of Scientific Instruments 85 083504

[3] Wei Y N, Yan W, Chen Z Y, Tong R H, Lin Z F, Zhang X L, Jiang Z H, Yang Z J, Ding Y H, Liang Y and J-TEXT team 2020 Dissipation of runaway current by massive gas injection on J-TEXT Plasma Phys. Control. Fusion 62 025002

[4] Huang D W, Chen Z Y, Tong R H, Yan W, Wang S Y, Wei Y N, Ma T K, Dai A J, Wang X L, Jiang Z H, Yang Z J, Zhuang G, Pan Y and J-TEXT Team 2017 Suppression of runaway current generation by supersonic molecular beam injection during disruptions on J-TEXT Plasma Phys. Control. Fusion 59 085002

[5] Jiang Z H, Wang X H, Chen Z Y, Huang D W, Sun X F, Xu T and Zhuang G 2016

Simulation of runaway electrons, transport affected by J-TEXT resonant magnetic perturbation Nucl. Fusion 56 092012
[6] Lin Z F, Chen Z Y, Huang D W, Huang J, Tong R, Wei Y N, Yan W, Li D, Hu Q M, Huang Y, Yang H Y, Li Y, Zhang X Q, Rao B, Yang Z J, Gao L, Ding Y H, Wang Z J, Zhang M, Liang Y, Pan Y, Jiang Z H and J-TEXT Team 2019 Full suppression of runaway electron generation by the mode penetration of resonant magnetic perturbations during disruptions on J-TEXT Plasma Phys. Control. Fusion 61 024005
[7] Liang Y, Wang N C, Ding Y H, Chen Z Y, Chen Z P, Yang Z J, Hu Q M, Cheng Z F, Wang L, Jiang Z H, Rao B, Huang Z, Li Y, Yan W, Li D, Liu H, Zeng L, Huang Y, Huang D W, Lin Z F, Zheng W, Hu F R, Zhao K J, Jiang M, Shi Y J, Zhou H, Peng S T, Guo W X, Gao L, Wang Z J, Zhang M, Yu K X, Hu X W, Yu Q, Zhuang G, Gentle K W, Pan Y and the J-TEXT Team 2019 Overview of the recent experimental research on the J-TEXT tokamak Nucl. Fusion 59 112016
[8] Sugihara M, Shimada M, Fujieda H, Gribov Y, Ioki K, Kawano Y, Khayrutdinov R, Lukash V and Ohmori J 2007 Disruption scenarios, their mitigation and operation window in ITER Nucl. Fusion 47 337–52
[9] Baylor L R, Combs S K, Duckworth R C, Lyttle M S, Meitner S J, Rasmussen D A and Maruyama S 2016 Pellet Injection Technology and Its Applications on ITER IEEE Trans. Plasma Sci. 44 1489–95
[10] Baylor L R, Combs S K, Foust C R, Jernigan T C, Meitner S J, Parks P B, Caughman J B, Fehling D T, Maruyama S, Qualls A L, Rasmussen D A and Thomas C E 2009 Pellet fuelling, ELM pacing and disruption mitigation technology development for ITER Nucl. Fusion 49 085013
[11] Hollmann E M, Aleynikov P B, Fülöp T, Humphreys D A, Izzo V A, Lehnen M, Lukash V E, Papp G, Pautasso G, Saint-Laurent F and Snipes J A 2015 Status of research toward the ITER disruption mitigation system Phys. Plasmas 22 021802
[12] Izzo V A and Parks P B 2017 Modeling of rapid shutdown in the DIII-D tokamak by core deposition of high-Z material Physics of Plasmas 24 060705
[13] Commaux N, Baylor L R, Jernigan T C, Hollmann E M, Parks P B, Humphreys D A, Wesley J C and Yu J H 2010 Demonstration of rapid shutdown using large shattered deuterium pellet injection in DIII-D Nucl. Fusion 50 112001
[14] Herfindal J L, Shiraki D, Baylor L R, Eidietis N W, Hollmann E M, Lasnier C J and Moyer R A 2019 Injection of multiple shattered pellets for disruption mitigation in DIII-D Nucl. Fusion 59 106034
[15] Shiraki D, Commaux N, Baylor L R, Eidietis N W, Hollmann E M, Lasnier C J and Moyer R A 2016 Thermal quench mitigation and current quench control by injection of mixed species shattered pellets in DIII-D Phys. Plasmas 23 062516
[16] Izzo V A 2013 Impurity mixing and radiation asymmetry in massive gas injection simulations of DIII-D Physics of Plasmas 20 056107
[17] Izzo V A, Whyte D G, Granetz R S, Parks P B, Hollmann E M, Lao L L and Wesley J C 2014 Magnetohydrodynamic simulations of massive gas injection into Alcator C-Mod and DIII-D plasmasa) Phys. Plasmas 10
[18] Izzo V A 2017 The effect of pre-existing islands on disruption mitigation in MHD simulations of DIII-D Physics of Plasmas 24 056102

[19] Pautasso G, Coster D, Eich T, Fuchs J C, Gruber O, Gude A, Herrmann A, Igochine V, Konz C, Kurzan B, Lackner K, Lunt T, Marascheck M, Mlynek A, Reiter B, Rohde V, Zhang Y, Bonnin X, Beck M and Prausner G 2009 Disruption studies in ASDEX Upgrade in view of ITER 12
[20] Reux C, Bucalossi J, Saint-Laurent F, Gil C, Moreau P and Maget P 2010 Experimental study of disruption mitigation using massive injection of noble gases on Tore Supra Nucl. Fusion 50 095006
[21] Lehnen M, Alonso A, Arnoux G, Baumgarten N, Bozhenkov S A, Brezinsek S, Brix M, Eich T, Gerasimov S N, Huber A, Jachmich S, Kruezi U, Morgan P D, Plyusnin V V, Reux C, Riccardo V, Sergienko G, Stamp M F and JET EFDA contributors 2011 Disruption mitigation by massive gas injection in JET Nucl. Fusion 51 123010
[22] Kim C C, Liu Y, Parks P B, Lao L L, Lehnen M and Loarte A 2019 Shattered pellet injection simulations with NIMROD Physics of Plasmas 26 042510
[23] Hu D, Nardon E, Lehnen M, Huijsmans G T A, van Vugt D C and JET Contributors 2018 3D non-linear MHD simulation of the MHD response and density increase as a result of shattered pellet injection Nucl. Fusion 58 126025
[24] Commaux N, Shiraki D, Baylor L R, Hollmann E M, Eidietis N W, Lasnier C J, Moyer R A, Jernigan T C, Meitner S J, Combs S K and Foust C R 2016 First demonstration of rapid shutdown using neon shattered pellet injection for thermal quench mitigation on DIII-D Nucl. Fusion 56 046007
[25] E.M. Hollmann, P.B. Parks, D. Shiraki, N. Alexander, N.W. Eidietis, C.J. Lasnier, and R.A. Moyer 2019 Demonstration of Tokamak Discharge Shutdown with Shell Pellet Payload Impurity Dispersal Phys. Rev. Lett. 122, 065001
[26] Fitzpatrick R 1998 Bifurcated states of a rotating tokamak plasma in the presence of a static error-field Physics of Plasmas 5 3325–41
[27] Haye R J L, Brennan D P, Buttery R J and Gerhardt S P 2015 Islands in the stream: The effect of plasma flow on tearing stabilitya) Phys. Plasmas 16 vol. 17, no. 5, 2010, Art. no. 056110
[28] V. A. Izzo and P. B. Parks, 2017 Modeling of rapid shutdown in the DIII-D tokamak by core deposition of high-Z material Phys. Plasmas 24, 060705
[29] Sovinec C R, Glasser A H, Gianakon T A, Barnes D C, Nebel R A, Kruger S E, Schnack D D, Plimpton S J, Tarditi A and Chu M S 2004 Nonlinear magnetohydrodynamics simulation using high-order finite elements Journal of Computational Physics 195 355–86
[30] Izzo V A and Joseph I 2008 RMP enhanced transport and rotational screening in simulations of DIII-D plasmas Nucl. Fusion 48 115004
[31] D. G. Whyte, T. E. Evans, A. G. Kellman, D. A. Humphreys, A. W. Hyatt, T. C. Jernigan, R. L. Lee, S. L. Luckhardt, P. B. Parks, M. J. Schaffer, and P. L. Taylor 1997 ENERGY BALANCE, RADIATION AND STABILITY DURING RAPID PLASMA TERMINATION VIA IMPURITY PELLET INJECTIONS ON DIII–D Proceedings of the 24th European Conference on Controlled Fusion and Plasma Physics (Berchtesgaden, Germany, 9–14 June 1997), vol 21A (Geneva: European Physical Society) p 1137
[32] Izzo V A, Parks P B, Eidietis N W, Shiraki D, Hollmann E M, Commaux N, Granetz R S, Humphreys D A, Lasnier C J, Moyer R A, Paz-Soldan C, Raman R and Strait E J 2015

The role of MHD in 3D aspects of massive gas injection Nucl. Fusion 55 073032
[33] Jiang Z H, Yang T T, Yuan J J, Li C H, Ye X, Huang J, Liang Y, Izzo V A, Huang M X, Tong R H, Huang Y, Cai Q X, Yan X T, Zhu L Z, Yang Z J, Ding Y H, Zhu P, Chen Z Y and J-TEXT 2020 Minor disruptions triggered by supersonic molecular beam injection on J-TEXT tokamak Nucl. Fusion 60 066004
[34] Lehnen M, Aleynikova K, Aleynikov P B, Campbell D J, Drewelow P, Eidietis N W, Gasparyan Yu, Granetz R S, Gribov Y, Hartmann N, Hollmann E M, Izzo V A, Jachmich S, Kim S-H, Kočan M, Koslowski H R, Kovalenko D, Kruezi U, Loarte A, Maruyama S, Matthews G F, Parks P B, Pautasso G, Pitts R A, Reux C, Riccardo V, Roccella R, Snipes J A, Thornton A J and de Vries P C 2015 Disruptions in ITER and strategies for their control and mitigation Journal of Nuclear Materials 463 39–48
[35] Tong R H, Chen Z Y, Jiang Z H, Zhang X L, Cheng Z F, Liu L Z, Li W, Yan W, Wei Y N, Lin Z F, Huang Y and Yang Z J 2018 Measurement of the toroidal radiation asymmetry during massive gas injection triggered disruptions on J-TEXT Review of Scientific Instruments 89 10E113